

# Line-of-sight shear in SLACS strong lenses

Natalie B. Hogg<sup>1\*</sup>, Anowar J. Shajib<sup>2,3</sup>, Daniel Johnson<sup>1</sup>, and Julien Larena<sup>1</sup>

<sup>1</sup> Laboratoire Univers et Particules de Montpellier, CNRS & Université de Montpellier, Parvis Alexander Grothendieck, Montpellier, France, 34090

<sup>2</sup> Department of Astronomy & Astrophysics, University of Chicago, Chicago, IL 60637, USA

<sup>3</sup> Kavli Institute for Cosmological Physics, University of Chicago, Chicago, IL 60637, USA

January 28, 2025

## ABSTRACT

**Context.** Inhomogeneities along the line of sight in strong gravitational lensing distort the images produced, in an effect called shear. If measurable, this shear may provide independent constraints on cosmological parameters, complementary to traditional cosmic shear.

**Aims.** We model 50 strong gravitational lenses from the Sloan Lens ACS (SLACS) catalogue with the aim of measuring the line-of-sight (LOS) shear for the first time. We use the ‘minimal model’ for the LOS shear, which has been shown to be theoretically safe from degeneracies with lens model parameters, a finding which has been confirmed using mock data.

**Methods.** We use the `dolphin` automated modelling pipeline, which uses the `lenstronomy` software as a modelling engine, to model our selected lenses. We model the main deflector with an elliptical power law profile, the lens light with elliptical Sérsic profiles and the source with a basis set of shapelets and an elliptical Sérsic profile.

**Results.** We successfully obtain a line-of-sight shear measurement from 18 of the 50 lenses. We find that these LOS shear measurements are consistent with external shears measured in recent works using a simpler shear model, which are larger than those expected from weak lensing. Neglecting the post-Born correction to the potential of the main deflector due to foreground shear leads to a propagation of degeneracies to the LOS shear measurement, and the same effect is seen if a prior is used to connect the lens mass and light ellipticities. The inclusion of an octupole moment in the lens mass profile does not lead to shear measurements that are in better agreement with the expectations from weak lensing.

**Key words.** Gravitational lensing: strong

## 1. Introduction

Gravitational lensing provides a unique window into the cosmology of our Universe on a wide range of scales. The strong lensing regime, in which a single massive deflector lenses a single source, has been used to measure the expansion rate of the Universe at  $z = 0$ ,  $H_0$  (Refsdal 1964; Wong et al. 2020; Birrer et al. 2020, 2024) via observations of the difference in arrival times of images of variable sources. Strong lensing has been used to probe properties of the lens galaxies, such as their density profiles (Treu et al. 2006; Shajib et al. 2021), and, by studying lens galaxies at different redshifts, their evolution over time (Chae 2010; Bezanson et al. 2011; Sahu et al. 2024). It has also been used to search for dark matter sub-haloes both within the main deflector halo and along the line of sight between the observer and lens (Vegetti & Koopmans 2009; Vegetti et al. 2012, 2014; Hezaveh et al. 2016; Nightingale et al. 2024).

The weak lensing regime probes larger scales. Unlike strong lensing, multiple images of the same source are not produced; rather, small distortions are induced on the single image of each source, artificially squashing and aligning them. The leading order shape distortion is shear, and its effect cannot be disentangled from the intrinsic shape of individual galaxies or their intrinsic alignment. The cosmic shear signal is detected by correlating the shapes of millions of galaxies in a given galaxy survey. Once extracted, cosmic shear can be used to place constraints on cosmological parameters like the matter density  $\Omega_m$  and the clustering

parameter  $\sigma_8$ . For a recent review of weak gravitational lensing, we refer the reader to Prat & Bacon (2025).

By virtue of their existence in our inhomogeneous Universe, strong lensing images will also experience weak lensing distortions, with Einstein rings in particular supplying the notion of a ‘standardisable shape’ from which shear may be robustly measured<sup>1</sup>, providing an alternative and independent probe of cosmology to the standard weak lensing shear. This idea was first investigated by Birrer et al. (2017), who modelled the lens COSMOS 0038+4133 with a shear model that consisted of four parameters: two components to describe the foreground shear as projected onto the lens plane, and two components to describe the background shear as projected onto the source plane. Whilst the shear parameters were shown to be constrained with high precision, this analysis revealed strong degeneracies between the shear parameters and the components of the ellipticity of the lens mass. This implies that, with this model, the constraints on the shear cannot be disentangled from the constraints on the lens mass, and the measurements cannot be safely used to obtain cosmological information.

Fleury et al. (2021) developed the minimal line-of-sight shear model to address this problem. Starting with three separate shears, the model exploits a source-position transformation to build a shear parameter, the ‘line-of-sight (LOS) shear’, which at leading order (i.e. for small values of the shear) is mathemat-

<sup>1</sup> In practice, shear can be recovered even when the image is not a complete Einstein ring, though the precision of the measurement may be degraded (Hogg et al. 2023).

\* e-mail: natalie.hogg@lupm.in2p3.fr.

ically free from degeneracy with any parameter used to describe the lens mass. The model fully describes the problem with the fewest possible parameters, and is therefore called the *minimal* LOS shear model – we will review the formalism behind this model in more detail below. Thanks to this freedom from degeneracies, it is the LOS shear in the minimal model which should be targeted for eventual cosmological inference. It was shown by Hogg et al. (2023) that the LOS shear is indeed free from degeneracies with lens model parameters using mock strong lensing images. It is therefore timely to attempt to measure this quantity in real strong lens imaging data.

This paper is organised as follows: in section 2 we review strong lensing theory and the minimal model; in section 3 we discuss the data used in this work and the method used to analyse it; in section 4 we present and discuss our results, and we conclude with section 5.

## 2. Strong lensing and the line-of-sight shear

In this section we review the strong lensing formalism and the derivation of the minimal model for the LOS shear. For full details, the reader is referred to Fleury et al. (2021).

The path of a light ray through the Universe is perturbed by the presence of massive objects. In the simplest possible case, there is a single deflector that perturbs the ray, with the angular position of the observed image  $\theta$  related to that of the unobserved source  $\beta$  via the lens equation,

$$\beta = \theta - \alpha(\theta), \quad (1)$$

where  $\alpha(\theta)$  is the displacement angle (also called the deflection angle), which depends on the gravitational potential of the deflector projected along the LOS into a single plane, i.e.

$$\alpha(\theta) = \frac{d\psi}{d\theta}, \quad (2)$$

where

$$\psi(\theta) \equiv \frac{D_{ds}}{D_{od}D_{os}} \hat{\psi}(D_{od}\theta), \quad (3)$$

and  $\hat{\psi}(\mathbf{x})$  is twice the projected gravitational potential produced by the surface density of the main lens,  $\Sigma(\mathbf{x})$ ,

$$\hat{\psi}(\mathbf{x}) \equiv \frac{4G}{c^2} \int d^2y \Sigma(\mathbf{y}) \ln |\mathbf{x} - \mathbf{y}|, \quad (4)$$

where  $\mathbf{x}$  is the vector describing the point where the light ray strikes the lens plane,  $G$  is Newton's constant and  $c$  the speed of light.

To a good approximation, further inhomogeneities beyond the main deflector can be treated as tidal perturbations, which induce a shear and convergence on the strong lens image. In this situation, Equation 1 becomes

$$\beta = \mathcal{A}_{os}\theta - \mathcal{A}_{ds} \frac{d\psi(\mathcal{A}_{od}\theta)}{d\theta}, \quad (5)$$

where the amplification matrices  $\mathcal{A}_{os}$ ,  $\mathcal{A}_{ds}$  and  $\mathcal{A}_{od}$  encapsulate the LOS perturbations between observer and source, main deflector and source, and observer and main deflector respectively. They can be parameterised as

$$\mathcal{A}_{ab} = \mathbf{1} - \Gamma_{ab}, \quad \Gamma_{ab} = \begin{bmatrix} \kappa_{ab} + \text{Re}(\gamma_{ab}) & \text{Im}(\gamma_{ab}) - \omega_{ab} \\ \text{Im}(\gamma_{ab}) + \omega_{ab} & \kappa_{ab} - \text{Re}(\gamma_{ab}) \end{bmatrix}, \quad (6)$$

where  $ab \in \{os, ds, od\}$  and  $\kappa_{ab}$  is the convergence,  $\gamma_{ab}$  the shear and  $\omega_{ab}$  the rotation of an image as seen at position  $a$  with respect to its source at  $b$ , produced by lens-lens coupling between the main deflector and the perturbers. A point regarding notation: we later denote the real component of any shear with  $\gamma_1$ , and the imaginary component with  $\gamma_2$ , with the magnitude  $\gamma = \sqrt{\gamma_1^2 + \gamma_2^2}$ .

Measuring the three individual shears  $\gamma_{os}$ ,  $\gamma_{ds}$  and  $\gamma_{od}$  from a strong lensing image is impossible, since they are degenerate with each other and with parameters of the model used to describe the gravitational potential of the main deflector,  $\psi(\theta)$  (Hogg et al. 2023); if the iso-potential contours are elliptical, there is an exact degeneracy between the ellipticity and the foreground shear  $\gamma_{od}$ . This is due to the fact that we have no access to the true, unlensed source position  $\beta$  or its unlensed morphology, meaning that up to linear transformations of the source, image positions are preserved; this is called the source-position transformation degeneracy (Schneider & Sluse 2014), which is a generalisation of the mass-sheet degeneracy (Falco et al. 1985).

However, this degeneracy can also be exploited in order to define a shear quantity which is measurable and free from degeneracies with lens model properties. This can be done by arbitrarily fixing a definition for  $\beta$ , analogous to lifting a gauge freedom by fixing the gauge. It was shown by Fleury et al. (2021) that a minimal model for LOS perturbations can be found by multiplying Equation 5 by  $\mathcal{A}_{od}\mathcal{A}_{ds}^{-1}$ , yielding

$$\tilde{\beta} = \mathcal{A}_{LOS}\theta - \frac{d\psi_{\text{eff}}}{d\theta}, \quad (7)$$

with the transformed source position  $\tilde{\beta} \equiv \mathcal{A}_{od}\mathcal{A}_{ds}^{-1}\beta$ , the LOS amplification matrix  $\mathcal{A}_{LOS} \equiv \mathcal{A}_{od}\mathcal{A}_{ds}^{-1}\mathcal{A}_{os}$  and the effective gravitational potential  $\psi_{\text{eff}}(\theta) \equiv \psi(\mathcal{A}_{od}\theta)$ . Equation 7 describes a main lens with potential  $\psi_{\text{eff}}$  and external tidal perturbations,  $\mathcal{A}_{LOS}$ , located in the same plane, and is equivalent to Equation 1 up to a source-position transformation. This means that we can consider  $\psi_{\text{eff}}$  as representative of the real physical potential of the main deflector,  $\psi$ , up to the same source-position transformation. The minimal model for LOS perturbations thus contains five meaningful parameters: the real and imaginary components of the foreground and LOS shears, and the LOS rotation term. The convergence parameters play no role, thanks to the mass-sheet degeneracy.

It was argued by Fleury et al. (2021) that the LOS shear, the combination  $\gamma_{LOS} \equiv \gamma_{od} + \gamma_{os} - \gamma_{ds}$  which arises from the  $\mathcal{A}_{LOS}$  amplification matrix in the minimal model, is not degenerate with the ellipticity of the main lens at leading order. This was further investigated by Hogg et al. (2023), who fit different models to a *Hubble* Space Telescope-like catalogue of mock strong lensing images, showing that  $\gamma_{LOS}$  is recoverable and non-degenerate with other lens model parameters, provided the lens mass model has a complexity equivalent to that which the mock images were generated with. The current work takes the logical next step, providing the first measurement of the LOS shear in real observational data, laying the groundwork for the cosmological constraints described above.

## 3. Data and methodology

In this section we describe the image data used, the components of our lens modelling and the method used to fit lens models to the images.

### 3.1. The strong lens sample

The Sloan Lens ACS (SLACS) strong lens catalogue is a large, well-studied sample of lenses, making it an ideal testbed for a first measurement of the LOS shear. Candidate lenses were identified spectroscopically in Sloan Digital Sky Survey (SDSS) data and followed up with *Hubble* Space Telescope (HST) observations (Bolton et al. 2006). The lenses we model in this work were imaged either with the Advanced Camera for Surveys (ACS) in the F555W filter or with the Wide Field and Planetary Camera 2 (WFPC2) in the F606W filter. The imaging data were obtained under the HST General Observers programmes 10494 (PI: Koopmans), 10798 (PI: Bolton), 10886 (PI: Bolton), and 11202 (PI: Koopmans).

A subset of 50 representative strong lenses from the SLACS catalogue were selected for study by Shajib et al. (2021), with the criteria that the chosen lenses should not have satellite galaxies or complex source morphologies, in order to allow an automated modelling procedure to be applied. Furthermore, lenses were selected that have imaging data in the F555W and F606W filters, as the deflector light tends to be fainter in these bands compared to the lensed source light, which makes it easier to deblend the source and deflector lights during lens modelling. Lastly, no disc-like lenses were selected.

The WFPC2 images were reduced for the original SLACS analysis; ACS images were reduced by Shajib et al. (2021) using the *Astrodrizzle* package (Avila et al. 2015), and the point-spread function (PSF) for each filter and camera combination were computed using *TinyTim* (Krist et al. 2011). In this work, we make use of these imaging data and PSFs, modelling the same 50 lenses as Shajib et al. (2021), thus enabling a direct comparison of our results with that previous work.

### 3.2. Mass and light models

We model the mass of the main deflector using the elliptical power law (EPL) profile of Tessore & Metcalf (2015). The convergence of this profile is given by

$$\kappa(x, y) = \frac{3 - \gamma^{\text{EPL}}}{2} \left( \frac{\theta_E}{\sqrt{qx^2 + y^2/q}} \right)^{\gamma^{\text{EPL}} - 1}, \quad (8)$$

where  $\theta_E$  is the Einstein radius,  $\gamma^{\text{EPL}}$  is the slope of the power law describing the three-dimensional mass distribution and  $q$  is the axis ratio of the ellipse. Whilst the EPL profile is a relatively simplistic choice to describe the lens mass, we use it in order to facilitate comparison of our results with other works that have also used it.

We model the light of the main deflector with two elliptical Sérsic profiles (Sérsic 1963, 1968). The surface brightness of a Sérsic profile is given by

$$I(x, y) = I_{\text{eff}} \exp \left[ k - k \left( \frac{\sqrt{qx^2 + y^2/q}}{R_{\text{eff}}} \right)^{1/n_S} \right], \quad (9)$$

where  $R_{\text{eff}}$  is the effective radius of the profile,  $I_{\text{eff}}$  is the surface brightness at that radius,  $q$  is the axis ratio,  $n_S$  is called the Sérsic index and  $k$  is a normalising constant such that  $R_{\text{eff}}$  is the half-light radius.

We use two Sérsic profiles rather than one to model the main deflector's light, as it has been shown, when fitting the specific lens RXJ1131-1231, that a single Sérsic profile results in significant residual differences between observation and model in the centre of the image (Claeskens et al. 2006; Suyu et al. 2013). We

constrain the profiles so that their centres share the same position in the lens plane, and furthermore, fix the Sérsic indices of the two profiles to one and four,  $n_S = 1$  and  $n_S = 4$ , representing an exponential and a de Vaucouleurs profile respectively (de Vaucouleurs 1948).

We model the light of the source with a further two light profiles: an elliptical Sérsic profile plus a set of shapelets. Shapelets are two-dimensional Gauss–Hermite polynomials, and thanks to their forming a complete basis set, any image can be decomposed into a linear combination of these polynomials (Refregier 2003). They have been used to measure weak lensing shear in galaxy images by Refregier & Bacon (2003), and for numerous source reconstructions from strong lensing images, beginning with Birrer et al. (2015).

We here summarise the shapelets formalism as presented in Refregier (2003). The dimensionless basis functions, or shapelets, are defined in one dimension as

$$\phi_n(x) \equiv \left[ 2^n \pi^{\frac{1}{2}} n! \right]^{-\frac{1}{2}} H_n(x) e^{-\frac{x^2}{2}}, \quad (10)$$

where  $H_n(x)$  is the Hermite polynomial of order  $n$ . A dimensional characteristic scale  $\beta$  can be introduced,

$$B_n(x; \beta) \equiv \beta^{-\frac{1}{2}} \phi_n(\beta^{-1}x), \quad (11)$$

where  $x$  has units of length, to preserve the dimensionlessness of the argument of  $\phi_n(x)$ . Then, the intensity of a light source  $f(x)$  can be decomposed into the basis functions

$$f(x) = \sum_{n=0}^{\infty} f_n B_n(x; \beta), \quad (12)$$

where  $f_n$  are the shapelet coefficients. To describe the intensity of light across an image, this formalism can be extended to two dimensions,  $\mathbf{x} = (x_1, x_2)$  and  $\mathbf{n} = (n_1, n_2)$ , in which case  $\phi_{\mathbf{n}}(\mathbf{x}) \equiv \phi_{n_1}(x_1)\phi_{n_2}(x_2)$  and  $B_{\mathbf{n}}(\mathbf{x}; \beta) \equiv \beta^{-1}\phi_{\mathbf{n}}(\beta^{-1}\mathbf{x})$ .

In practice, the parameters of our set of shapelets are the maximum order for the Hermite polynomial  $n_{\text{max}} \geq n_1 + n_2$ , which in turn determines the number of shapelets in the set,  $N_{\text{shapelets}} = (n_{\text{max}} + 1)(n_{\text{max}} + 2)/2$ , and the characteristic scale  $\beta$ . In our analysis, we fix  $n_{\text{max}} = 6$ , whilst  $\beta$  is inferred by the Markov chain Monte Carlo (MCMC) procedure described below. The centre of the set of shapelets is constrained to be at the same position in the source plane as the centre of the elliptical Sérsic profile which makes up the rest of the source light model.

### 3.3. Shear models

We use three different models for the shear of the strong lensing images. The first is the minimal LOS shear model, described by Equation 7. In this case, the shear model has five parameters: the LOS shear parameters  $\gamma_1^{\text{LOS}}$  and  $\gamma_2^{\text{LOS}}$ , the foreground shear parameters  $\gamma_1^{\text{od}}$  and  $\gamma_2^{\text{od}}$  and the LOS rotation parameter  $\omega_{\text{LOS}}$ .

In Hogg et al. (2023), it was shown that when fitting lens models to mock data, the original image could be recovered even when the foreground shear was neglected in  $\psi_{\text{eff}}$ . In the second shear model we consider, we omit the explicit appearance of  $\gamma_{\text{od}}$  in the effective main-lens potential. The foreground shear term physically corresponds to the effect of post-Born corrections in the main deflection – in the presence of foreground perturbations, light rays do not hit the main lens plane at the same position as if those perturbations were absent. Thus, the omission of the foreground shear must be understood as the assumption that such post-Born corrections are degenerate enough with the

parameters of the main lens to be absorbed in them; we do not assume that foreground shear, nor its post-Born effect on the main deflector, are negligible. Practically speaking, this means that we fix  $\gamma_1^{\text{od}} = \gamma_2^{\text{od}} = 0$  in our analysis using this model, which we refer to as the ‘no foreground shear model’ throughout the rest of this paper.

The final shear model we consider is a further restriction of the above, created by fixing the LOS rotation to zero,  $\omega_{\text{LOS}} = 0$ . This model is mathematically equivalent to the ‘external’ or ‘residual’ shear model widely used in the literature (Tan et al. (2024); see Shajib et al. (2024) for a discussion of this terminology), and has two parameters,  $\gamma_1^{\text{LOS}}$  and  $\gamma_2^{\text{LOS}}$ . We fit the strong lenses with this model to allow us to make a direct comparison with shear values previously reported in the literature for these lenses. We refer to this model as ‘external shear equivalent’.

We note that in practice, what is actually measured in each of these cases is the ‘reduced shear’,  $g_{\text{ab}} = \gamma_{\text{ab}}/(1 - \kappa_{\text{ab}})$ . The convergence  $\kappa_{\text{ab}}$  is typically small (and in fact, unmeasurable in strong lensing due to the mass-sheet degeneracy),  $\kappa_{\text{ab}} \ll 1$ , meaning that we can approximate  $g_{\text{ab}} \approx \gamma_{\text{ab}}$ . Throughout the rest of this work, we will therefore refer to what is technically ‘reduced shear’ as ‘shear’.

### 3.4. The automated modelling procedure

Before beginning the modelling, we apply a custom annular mask to each of our 50 selected SLACS lenses, with an inner radius of  $0.4''$  and an outer radius selected manually for each lens (typically around  $3.0''$ ) masking out the central and outer regions of the images. We also mask the light from any prominent foreground object in the field of view. This masking is an alternative to the lens light removal, for example via a multi-Gaussian expansion, that is performed in other analyses, e.g. He et al. (2024). However, when the mask is in place, we still model the remaining lens light, allowing us to infer the uncertainties in the model parameters. This cannot be done when the lens light is removed before any modelling step.

We then fit lens models to the images using the `lenstronomy` package (Birrer & Amara 2018; Birrer et al. 2021), via the `dolphin` software (Shajib et al. 2021; Tan et al. 2024), which provides an automated modelling pipeline to uniformly model a large sample of lenses. The modelling has two stages: first, a particle swarm optimisation (PSO) is used to locate the maximum likelihood value for each parameter in the model, i.e. the lens mass, lens light and source light parameters.

The `dolphin` package provides a recipe to increase the computational efficiency of the optimisation step, in which the lens mass, lens light and source light model parameters are individually optimised whilst the rest of the parameters are kept fixed, before all the model parameters are optimised together. Full details of this optimisation recipe can be found in Shajib et al. (2021).

In the second stage of the parameter inference, an MCMC method is used to sample from the posterior distribution formed by the likelihood and the user-defined priors for each parameter. In this work we use the affine-invariant ensemble sampling algorithm provided by the `emcee` package (Goodman & Weare 2010; Foreman-Mackey et al. 2013); the ensemble of walkers is initialised in a small Gaussian ball around the maximum likelihood value found by the PSO. Our chosen priors are listed in Table 1.

Besides the priors on the individual parameters, `dolphin` offers the user the possibility to add other prior constraints on the parameters. In particular, a limit can be imposed on the maximum difference between the orientation of the lens mass and lens

**Table 1.** Priors on the model parameters. The prior distributions are uniform between the stated limits.

| Component    | Parameter               | Prior             |
|--------------|-------------------------|-------------------|
| Lens mass    | $\theta_{\text{E}}$     | $[0.03'', 3'']$   |
|              | $\gamma^{\text{EPL}}$   | $[1.3, 2.8]$      |
|              | $e_1$                   | $[-0.5, 0.5]$     |
|              | $e_2$                   | $[-0.5, 0.5]$     |
|              | $x$                     | $[-0.5'', 0.5'']$ |
| Lens light   | $y$                     | $[-0.5'', 0.5'']$ |
|              | $R_{\text{eff}}$        | $[0.1, 5.0]$      |
|              | $e_1$                   | $[-0.5, 0.5]$     |
|              | $e_2$                   | $[-0.5, 0.5]$     |
|              | $x$                     | $[-0.5'', 0.5'']$ |
| Source light | $y$                     | $[-0.5'', 0.5'']$ |
|              | $\beta$                 | $[0.02'', 0.2'']$ |
|              | $R_{\text{eff}}$        | $[0.04'', 0.5'']$ |
|              | $n_{\text{S}}$          | $[0.5, 8.0]$      |
|              | $e_1$                   | $[-0.5, 0.5]$     |
| Shear        | $e_2$                   | $[-0.5, 0.5]$     |
|              | $x$                     | $[-0.2'', 0.2'']$ |
|              | $y$                     | $[-0.2'', 0.2'']$ |
|              | $\gamma_1^{\text{od}}$  | $[-0.5, 0.5]$     |
|              | $\gamma_2^{\text{od}}$  | $[-0.5, 0.5]$     |
| Shear        | $\gamma_1^{\text{LOS}}$ | $[-0.5, 0.5]$     |
|              | $\gamma_2^{\text{LOS}}$ | $[-0.5, 0.5]$     |
|              | $\omega_{\text{LOS}}$   | $[-0.5, 0.5]$     |

light ellipticities, as well as a limit on the ratio of the axis ratio of the lens mass and lens light. These priors reflect the physical expectation that the underlying matter distribution in a galaxy will trace the visible light.

However, this is only true for objects with a relatively insignificant foreground; if a non-negligible foreground is present, the lens light itself will undergo potentially significant lensing by that foreground. In this case, a prior rigidly joining lens light and lens mass ellipticity is no longer physically well-motivated, and the degeneracies present between foreground shear,  $\gamma_{\text{od}}$ , and the lens mass ellipticity will lead to biased or simply incorrect parameter inference across the model; see Johnson et al. (2024) for further discussion of foreground biases in strong lensing. We will show an example of this below; in general, we recommend that, given the entanglement between foreground effects and the lens model, this type of prior should not be used when attempting

to infer LOS shear in the minimal model (as this model contains  $\gamma_{\text{od}}$ ).

The benefits of this kind of automated modelling procedure where the same model is fit to every lens are that the required investigator time is minimised, as it obviates the need for manual modelling of individual lenses to fine-tune the setup (which would anyway be infeasible even for a modest-size lens catalogue, e.g. over 500 lenses), and that results from individual fits are more readily comparable. On the other hand, whilst the strong lensing cross-section is dominated by elliptical galaxies (Turner et al. 1984), there is bound to be a potentially significant number of lenses that cannot be satisfactorily modelled by a ‘one size fits all’ approach. As we will see, this accounts for a significant fraction of the lenses we attempted to model in this work.

## 4. Results and discussion

The above-described automated modelling procedure allowed us to successfully model 18 of the initial 50 lenses with the minimal model. We rejected eight fits due to the LOS shear parameters  $\gamma_1^{\text{LOS}}$  and  $\gamma_2^{\text{LOS}}$  being unconstrained, a further thirteen fits due to the presence of strong residuals between the model and the data, and a further three fits due to the best-fit value of the slope of the elliptical power law potential being atypically shallow,  $\gamma^{\text{EPL}} \leq 1.4$ . Note that the remaining eight lenses of the initial 50 were successfully modelled with the no foreground shear or external shear models, but not the minimal model, which we will discuss in more detail below.

Small values of  $\gamma^{\text{EPL}}$  result in central images in the lens model which would never be observable in reality due to the light emitted by the deflector, but since we mask out the centre of each image during our modelling, the absence of corresponding central images in the data are not penalised (Shajib et al. 2021). We therefore choose to remove the three cases where  $\gamma^{\text{EPL}}$  has converged to a very small value *a posteriori*.

### 4.1. LOS shear in the minimal model

We firstly present the 18 lenses in which the LOS shear was successfully measured using the minimal LOS shear model. The observed image, reconstructed image, normalised residuals between data and model, reconstructed source and joint marginalised posterior distribution of the LOS shear parameters  $\gamma_1^{\text{LOS}}$  and  $\gamma_2^{\text{LOS}}$  are shown in the five respective columns of Figure 1, Figure 2 and Figure 3 for each of the 18 lenses. Furthermore, the reduced  $\chi^2$  of each model is shown in the upper left part of each panel in the second column, and the measurement of the shear magnitude  $\gamma_{\text{LOS}}$  and the associated  $1\sigma$  uncertainty is shown in each panel of the last column. We use the ChainConsumer package (Hinton 2016) to analyse our MCMC chains; we present the posterior distributions after the removal of the first 20% of the chain as burn-in.

We note that the reduced  $\chi^2$  for the majority of our models, i.e. the  $\chi^2$  normalised by the number of degrees of freedom in the model, is less than one. This usually indicates overfitting; in other words, the number of parameters in the model is so large that the noise is being fit. However, we must be cautious not to over-interpret the reduced  $\chi^2$  values, as we do not compute the uncertainty on these numbers. For a rough estimation, we may approximate the  $\chi^2$  distribution as a Gaussian, allowing us to estimate its standard deviation as  $\sigma_{\chi^2} \approx \sqrt{2/N}$ , where  $N$  is the number of samples (Andrae et al. 2010). For our 18 successfully

fit lenses,  $\sigma_{\chi^2} \approx \sqrt{2/18} = 0.33$ , meaning that all but two of our reduced  $\chi^2$  values are consistent with one at  $1\sigma$ .

In all of the lenses shown here, the magnitude of the LOS shear is found to be distinct from zero by at least  $1\sigma$ . We can compare the distribution of the measured LOS shear with ‘external’ or ‘residual’ shear measured in other works. We select the shear measurements in Shajib et al. (2021), Etherington et al. (2022) and Tan et al. (2024), as these three works study similar lens samples to those in this work, using the same or similar modelling pipelines. The samples do not directly overlap; we model eight lenses successfully that were not successfully modelled by Shajib et al. (2021), of which three were also not successfully modelled by Tan et al. (2024): SDSSJ0959+4416, SDSSJ1016+3859 and SDSSJ1020+1122. We successfully modelled five lenses that were not successfully modelled by Etherington et al. (2022); these were all successfully modelled by either Shajib et al. (2021) or Tan et al. (2024).

In Figure 4 we show histograms of the measurements of the shear magnitude in this work ( $\gamma_{\text{LOS}}$ ) and from the aforementioned other works ( $\gamma_{\text{ext}}$ ). The top row shows the distributions of all the shear measurements from those works, whilst the bottom row shows the distributions of the shear measurements from just those lenses which we modelled successfully with the minimal LOS shear model in this work.

We can see from this figure that when comparing to the full distributions of shear measurements (solid colour histograms), the distribution of the measured LOS shear magnitude (black) is somewhat broader than the measurements of the external shear magnitude from the three works we compare with. The LOS shear distribution has a longer tail reaching to larger shear magnitudes, except for one outlying point in the Etherington et al. (2022) measurements. Furthermore, the peak of the LOS shear distribution is at a larger magnitude than the external shear from the works we compare with. The same holds true for the comparison with the shears from only those lenses which match those modelled by the minimal model in this work (coloured hatched histograms).

To quantify the differences in the distributions, we can use the  $k$ -sample Anderson–Darling (AD) test (Anderson & Darling 1952), which tests whether a number of different samples are drawn from the same underlying population. The test is similar to the Kolmogorov–Smirnov test (Sprenth 1998), but is more sensitive to differences in the tails of the sample distributions (Razali & Wah 2011). This is appropriate for our distributions of measured shear. We run the AD test three times, comparing the distribution of the LOS shear magnitudes with the distribution of the external shear magnitudes in Shajib et al. (2021), Etherington et al. (2022) and Tan et al. (2024). We use only the shears as measured from the same lenses modelled in this work.

At 5% significance level, i.e. approximately  $2\sigma$ , the null hypothesis that the two samples are drawn from the same underlying distribution is rejected for the shears measured in Shajib et al. (2021), but cannot be rejected in the other two cases. From this, we conclude that the information contained in measurements of the shear parameter in the minimal model does not differ from that contained in the external shear to a statistically significant level, in the lenses studied in this work.

### 4.2. Neglecting foreground shear and LOS rotation

Given this finding, the role of the foreground shear  $\gamma_{\text{od}}$  and the LOS rotation,  $\omega_{\text{LOS}}$ , may be questioned. If the distribution of LOS shear is statistically indistinguishable from distributions of

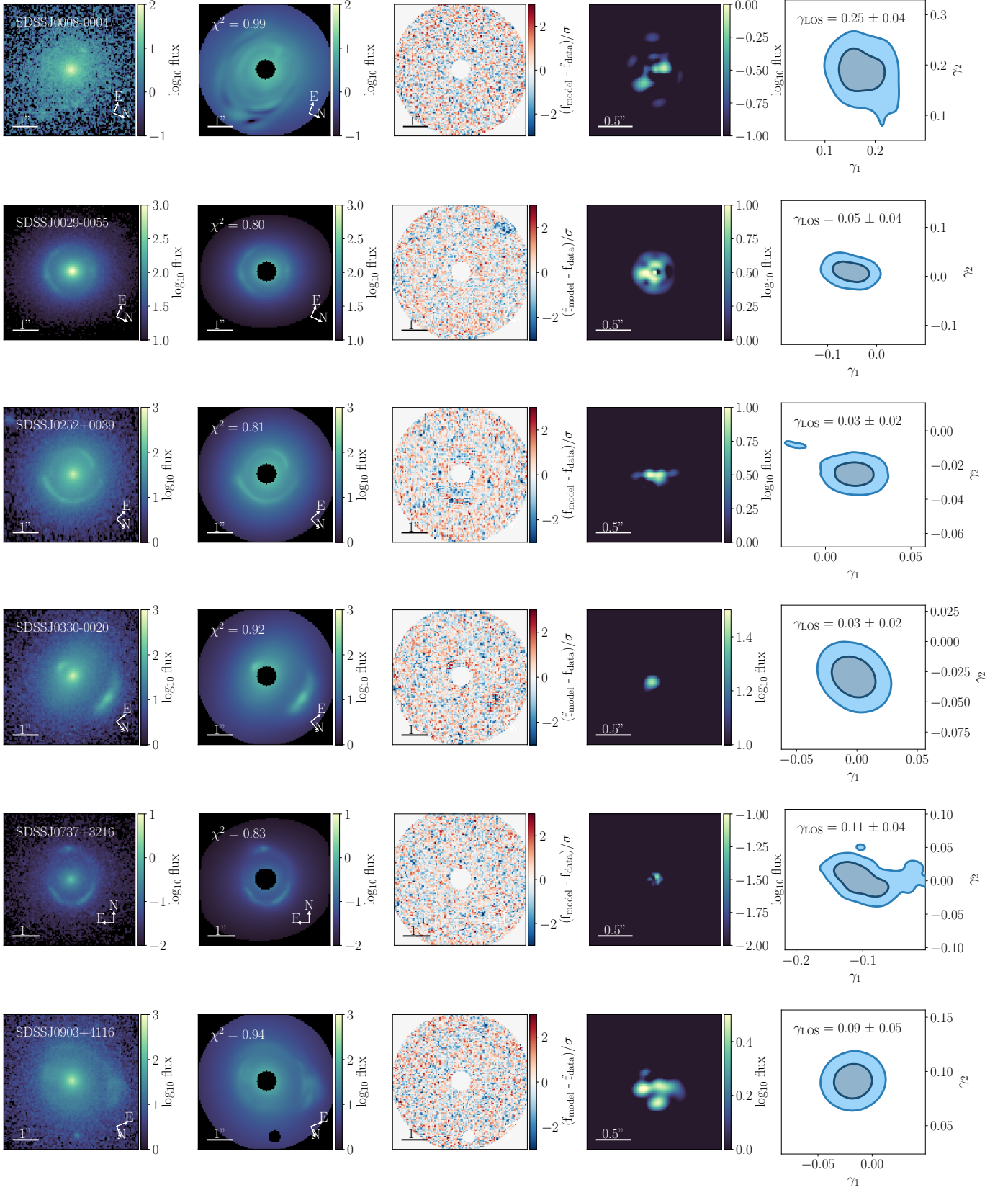


**Fig. 1.** The first six lenses fit successfully with the minimal model. From left to right, the panels show the single-band image data for each lens, our reconstruction of the image along with the reduced  $\chi^2$  of the model, the residual difference between the image and the reconstruction, the reconstructed source and the joint posterior distribution of the components of the LOS shear,  $\gamma_1$  and  $\gamma_2$ . The dark and light shaded areas are respectively the  $1\sigma$  and  $2\sigma$  confidence intervals.

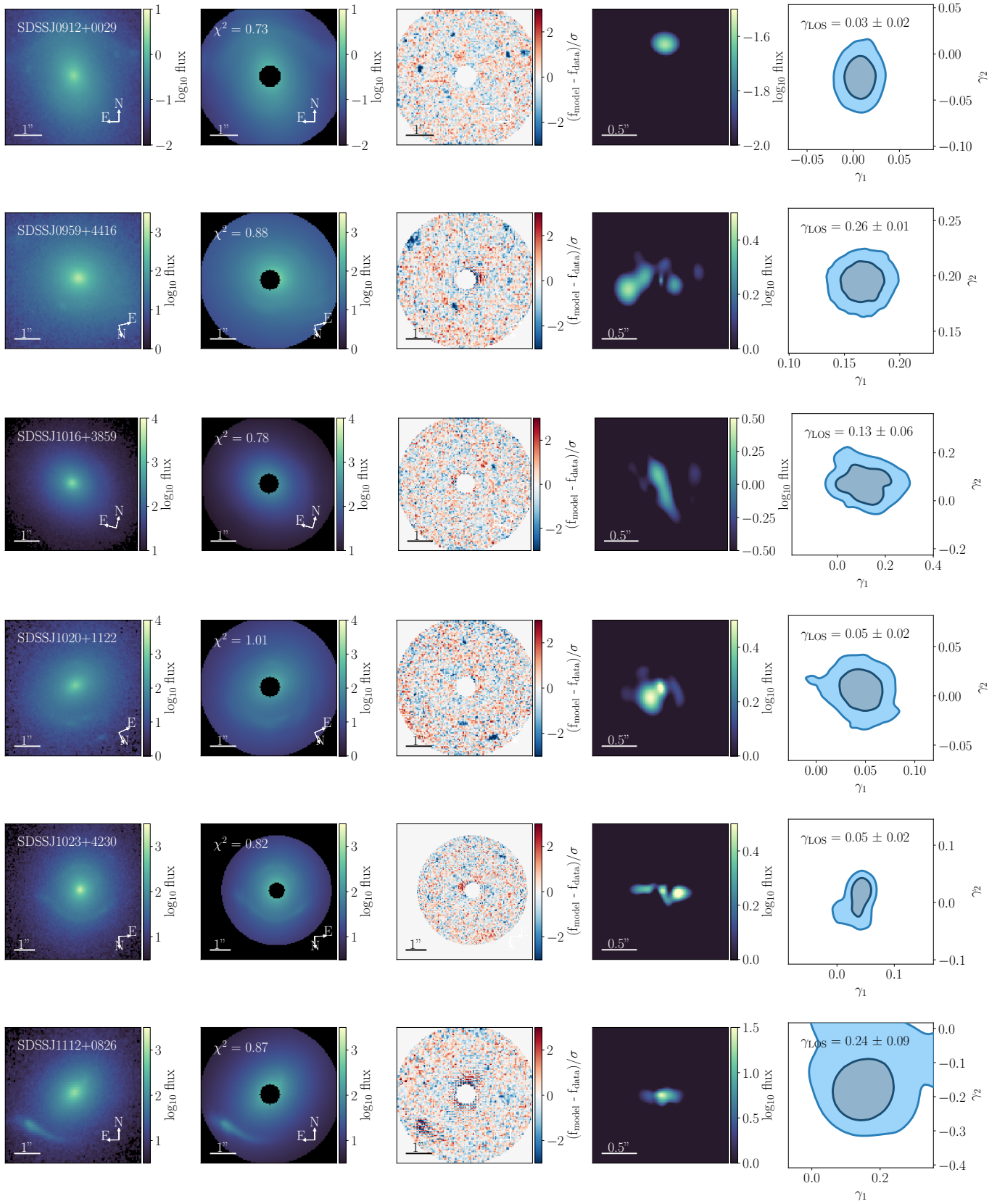


**Fig. 2.** The next six lenses fit successfully with the minimal model. From left to right, the panels show the single-band image data for each lens, our reconstruction of the image along with the reduced  $\chi^2$  of the model, the residual difference between the image and the reconstruction, the reconstructed source and the joint posterior distribution of the components of the LOS shear,  $\gamma_1$  and  $\gamma_2$ . The dark and light shaded areas are respectively the  $1\sigma$  and  $2\sigma$  confidence intervals.

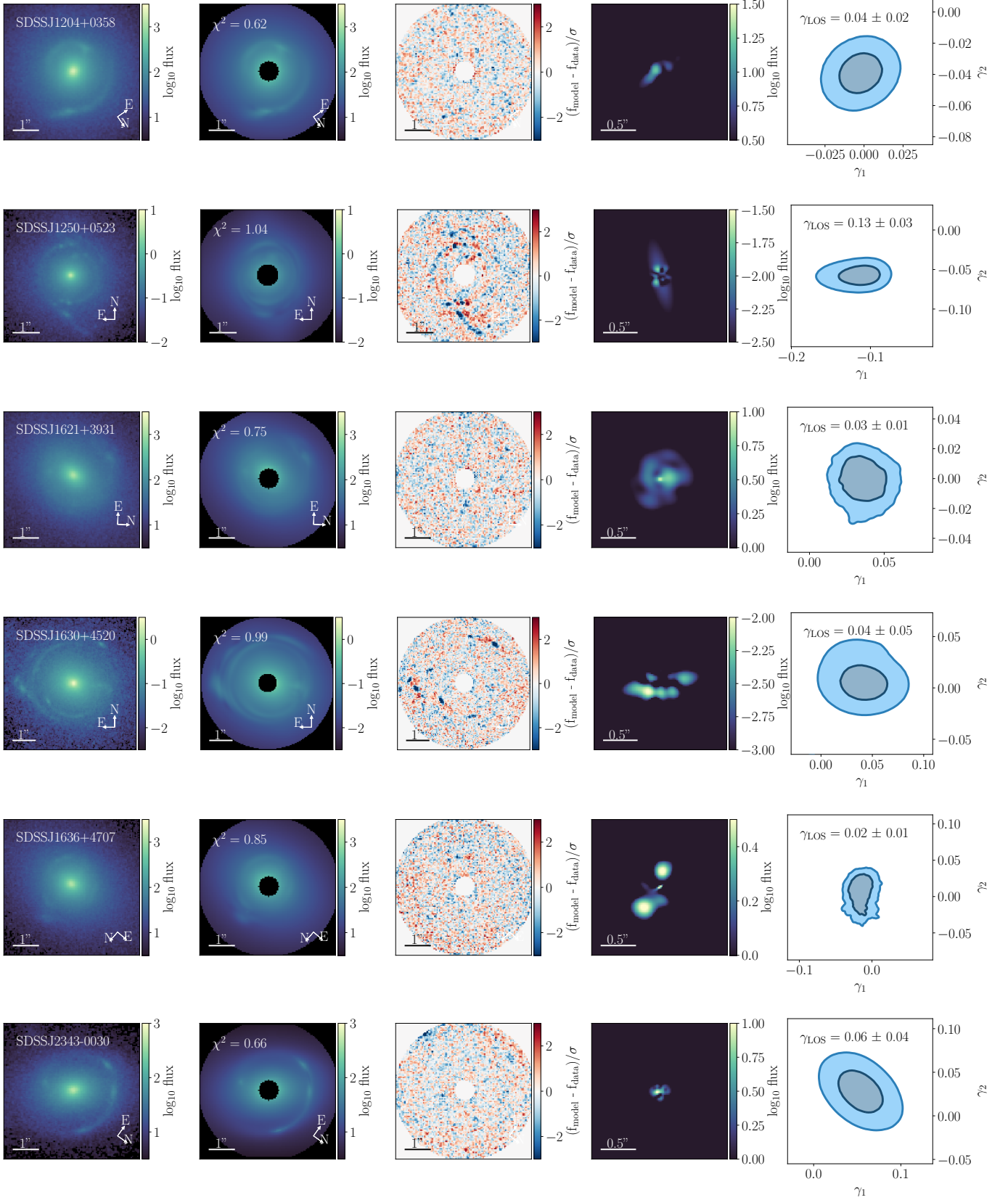


**Fig. 3.** The last six lenses fit successfully with the minimal model. From left to right, the panels show the single-band image data for each lens, our reconstruction of the image along with the reduced  $\chi^2$  of the model, the residual difference between the image and the reconstruction, the reconstructed source and the joint posterior distribution of the components of the LOS shear,  $\gamma_1$  and  $\gamma_2$ . The dark and light shaded areas are respectively the  $1\sigma$  and  $2\sigma$  confidence intervals.

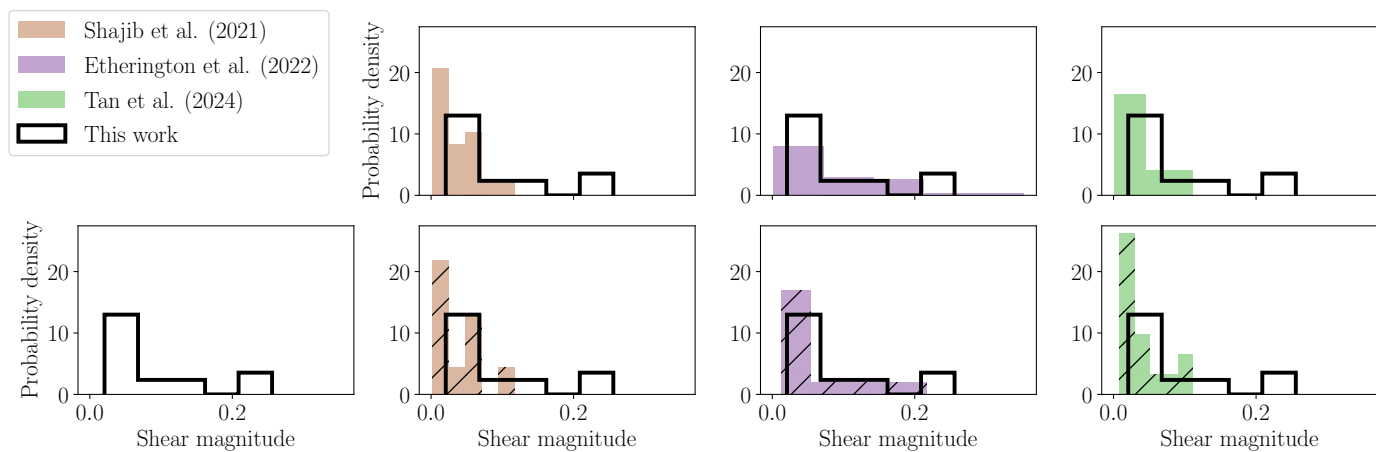


**Fig. 4.** Histograms of shear magnitude measurements. The three panels in the top row (solid colour histograms) show the external shear as measured in the cited works. The open black histograms show the LOS shear as measured in this work. The bottom row (hatched coloured histograms) show the measurements of external shear from the same lenses as the minimal model was successful at fitting in this work.

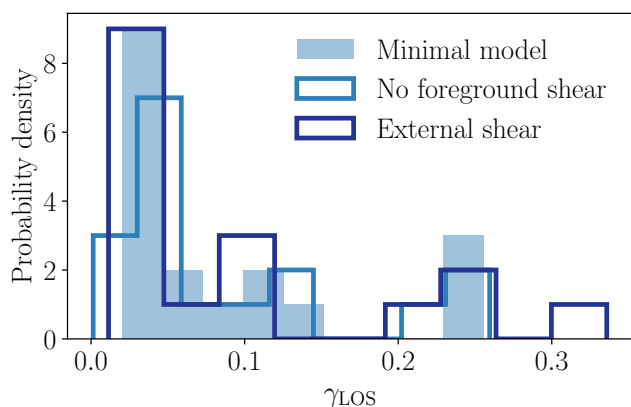


**Fig. 5.** Measured LOS shear in the minimal model (solid blue), no foreground shear model (unfilled light blue) and external shear equivalent model (unfilled dark blue).

external shear found in other studies, what value do the additional three parameters bring? We can explore this question by re-fitting the same strong lenses but with the foreground shear fixed to zero, and again with both the foreground shear and LOS rotation fixed to zero. The latter model is mathematically equivalent to the external shear model, as it contains only two parameters to describe the shear effect,  $\gamma_1^{\text{LOS}}$  and  $\gamma_2^{\text{LOS}}$ .

Our first finding is that seven more lenses on top of the 18 fit with the minimal model were able to be modelled successfully in the no foreground shear model, and four more lenses with the external shear equivalent model, of which three lenses are common to both sets. Six of these fits were rejected in the case of the minimal model due to the LOS shear components being unconstrained; the remaining two had very small best-fit values of the EPL slope. This finding implies that, as is commonly known, the reduction in parameter space may bring a marginal improvement in the sampling of the MCMC; fewer parameters means that the joint posterior distribution is simpler and potentially easier to sample from, leading to better convergence.

In Figure 5 we show the distributions of the measured LOS shear in the minimal model, no foreground shear and external shear equivalent models. The distributions are broadly similar

in shape, implying that the reduction in parameter space does not significantly change the measured LOS shear distribution, as expected from the comparison between our results and the literature. The two-sample AD test does not reject the null hypothesis that the samples were drawn from the same underlying distribution as the minimal model in either case.

Next, we can examine the posterior distributions of the lens ellipticity and shear parameters to understand how the degeneracies between these quantities behave in each model. As an example, in Figure 6, we show the marginalised posterior distributions on the lens mass ellipticity, foreground shear, LOS shear and LOS rotation in the minimal model, no foreground shear model and external shear equivalent model as fit to lens SDSS03300-0020.

From this figure, the extremely strong degeneracy between the lens mass ellipticity and foreground shear can be seen in the minimal model (blue contours). Removal of the foreground shear from the model (purple contours) leads to spuriously tight constraints on the ellipticity of the lens mass. The degeneracy between the foreground shear and the lens mass ellipticity is propagated to the LOS shear, leading to a significantly different LOS shear measurement. In this lens, the degeneracy is particularly apparent between  $\gamma_1^{\text{LOS}}$  and  $e_1^{\text{mass}}$ , whilst the central values of the  $\gamma_2^{\text{LOS}}$  posteriors change significantly between the minimal and no foreground shear models.

This finding is in sharp contrast with the results of Hogg et al. (2023), which demonstrated that, in mock data, neglecting the foreground shear in the model had little effect on the inferred LOS shear. However, we are now considering a far more complex model applied to real data. Somewhat surprisingly, when the LOS rotation is removed from the model (green contours), the LOS shear constraint is once again in agreement with the minimal model.

To examine whether this effect is systematic across all the lenses studied in this work, we can look at the LOS shear magnitudes measured in the minimal model compared to those measured in the no foreground shear and external shear equivalent models. In Figure 7 we show these measurements plotted against each other; the minimal model against the no foreground shear model in the left panel and the minimal model against the external shear equivalent model in the right panel.

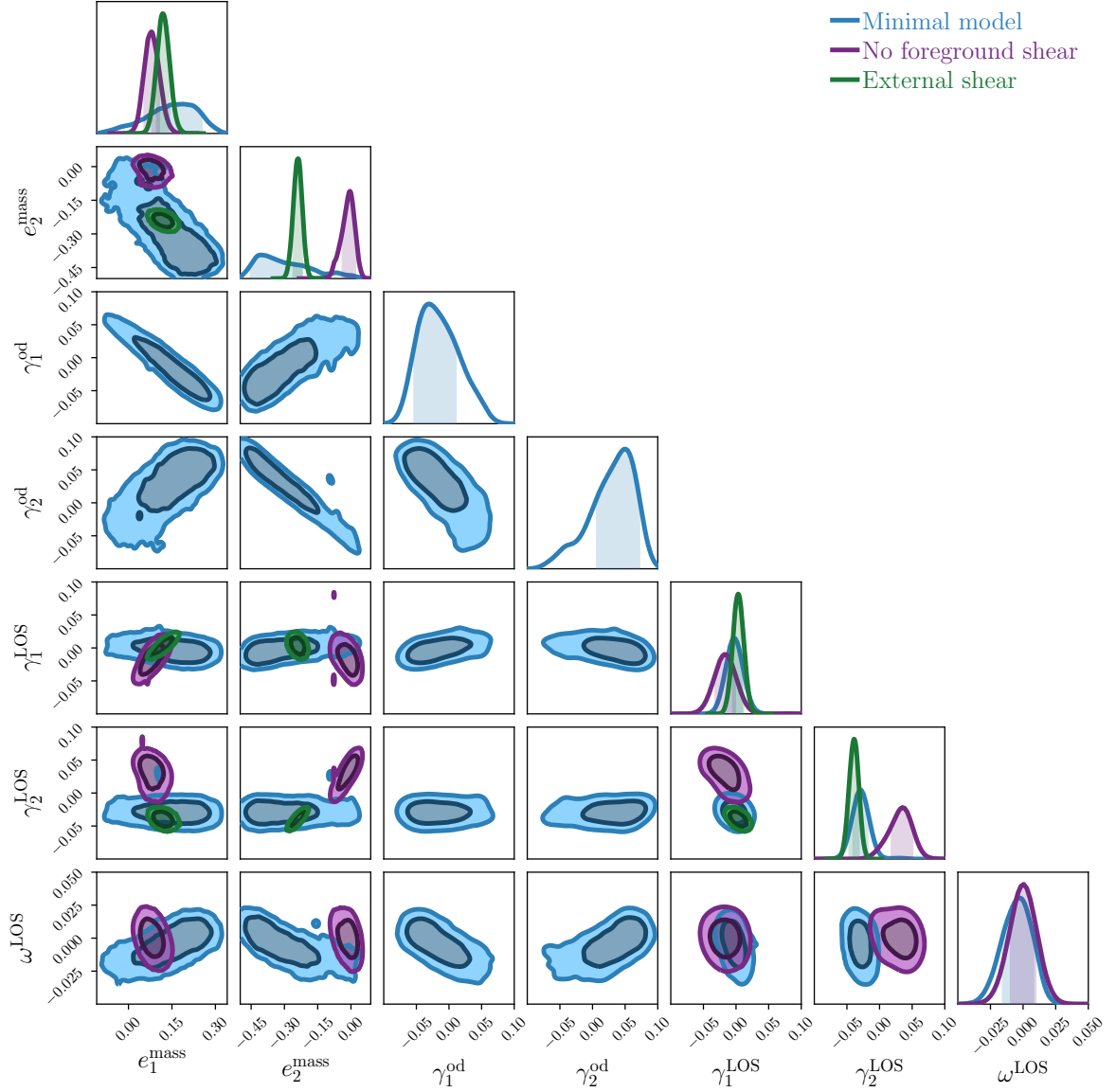


**Fig. 6.** The one and two dimensional marginalised posterior distributions on the lens mass ellipticity, foreground shear, LOS shear and LOS rotation parameters obtained by fitting, as an example, lens SDSSJ0330-0020 with the minimal model (blue), no foreground shear model (purple) and external shear equivalent model (green). Dark and light shaded regions represent the  $1\sigma$  and  $2\sigma$  confidence intervals respectively.

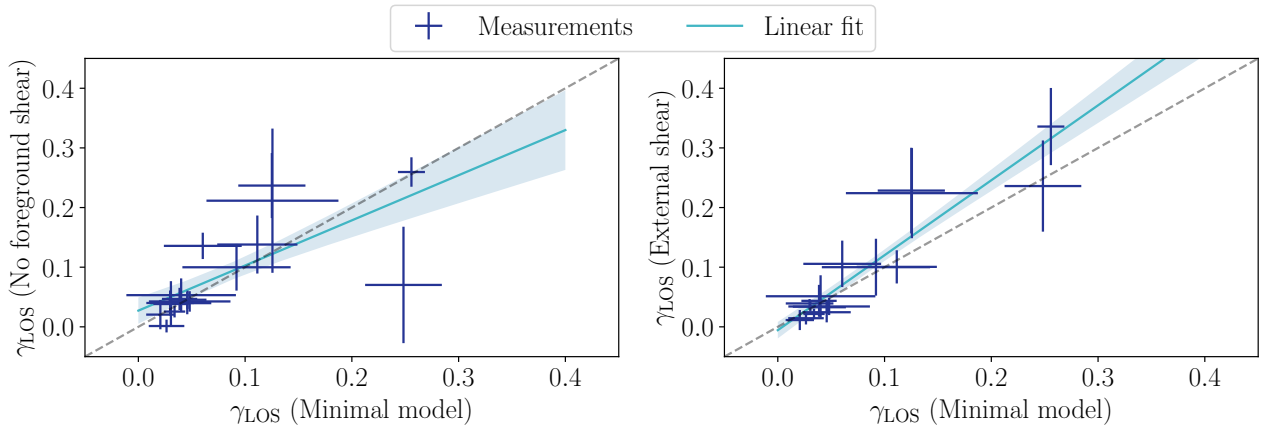


**Fig. 7.** *Left:* LOS shear magnitudes in the minimal model plotted against the LOS shear magnitudes in the no foreground shear model (blue crosses). *Right:* LOS shear magnitudes in the minimal model plotted against the LOS shear magnitudes in the external shear equivalent model (blue crosses). The dashed grey lines represent the  $y = x$  line whilst the solid blue lines show a linear fit to the measurements, with a  $1\sigma$  shaded region. The fits are  $y = 0.76x + 0.02$  and  $y = 1.23x - 0.01$  respectively. The error bars on the points are the  $1\sigma$  standard deviations.

Computing a linear fit<sup>2</sup> to the scatter shows that, for large shear values ( $\gamma_{\text{LOS}} > 0.1$ ), the LOS shear magnitude measured in the no foreground shear model tends to be slightly smaller than what would be measured in the minimal model, whilst for small values of the shear, the results from the two models are consistent. Conversely, the LOS shear magnitude measured in the external shear model tends to be larger than what would be expected from the minimal model, again for large shear values.

The slope of the fit being less than one in the comparison between the minimal model and no foreground shear model is driven by the one clear outlying point at  $\gamma_{\text{LOS}} = 0.25$  in the minimal model and  $\gamma_{\text{LOS}} = 0.07$  in the no foreground shear model. Removing this point results instead in a slope greater than one, similar to that seen when comparing the minimal model with the external shear model.

Furthermore, this figure reveals that the uncertainty on the measured LOS shear magnitude tends to increase as the magnitude itself increases. Due to the small number of points and their relatively large uncertainties, we note that this conclusion may not be borne out if a larger number of more accurate measurements were to be achieved.

We may conclude here that, when considering a single strong lens, a measurement of LOS shear has the potential be significantly affected by neglecting foreground shear and rotation, and the subsequent inheritance of a degeneracy between the LOS shear parameters and the lens mass ellipticity parameters. The difference between the models is negligible for small inferred shear values but grows with the magnitude of the shear. It is therefore apposite to investigate possible causes of these large shear values.

### 4.3. Adding boxyness and diskyness

Etherington et al. (2024) showed that the large values of shear measured from strong lensing are inconsistent with expectations from weak lensing measurements, both in mock data and in observations, a study which was conducted using the external shear model. We are able to make an independent confirmation of this finding for LOS shear using  $N$ -body simulations.

We use the RAYGALGROUPSIMS suite of relativistic  $N$ -body simulations, whose publicly available data contains weak lensing maps that include post-Born effects, magnification bias and redshift-space distortions (Rasera et al. 2022). The maps provide convergence and shear measurements at a given set of redshifts, between which we can interpolate to compute  $\gamma_{\text{os}}$ ,  $\gamma_{\text{od}}$  and  $\gamma_{\text{ds}}$  shear values for any given deflector and source redshift. From these, we compute the expected  $\gamma_{\text{LOS}}$  for any line of sight in the simulation, and thus produce a distribution of expected  $\gamma_{\text{LOS}}$  shear magnitudes.

In Figure 8, we show the distribution of the two LOS shear components  $\gamma_1^{\text{LOS}}$  and  $\gamma_2^{\text{LOS}}$ , as well as the magnitude of the LOS shear  $\gamma_{\text{LOS}}$  as estimated from the RAYGALGROUPSIMS (unfilled black histograms) along with the measurements from the SLACS lenses (solid blue histograms). Looking first at the distributions of the two individual shear components, we do not see a stark

<sup>2</sup> To do this, we use the ordinary least squares fitting method provided by `numpy.polyfit`. However, least squares fitting becomes inaccurate when the independent variable has significant uncertainties, as is the case here (Fuller 1987). We further choose not to weight the fit using the uncertainty on the dependent variable in either case. The displayed uncertainty on each linear fit (shaded blue region) is therefore computed from the covariance matrix returned by `numpy.polyfit` based solely on the shear values, without their errors.

difference between the simulated and observed shears; in particular, the peaks of the distributions are in good agreement. There remains a clear difference in the tails of the simulated and observed distributions of both shear components.

Examining instead the shear magnitude, the significant difference between the shear estimated from the simulations and the shear observed in the strong lenses is clearly apparent, in agreement with the findings of Etherington et al. (2024). The two-sample AD test rejects the null hypothesis that the two samples (simulated and observed) are drawn from the same underlying distribution at 95% confidence.

It therefore seems possible that there is some contribution to the LOS shear from the local environment of the lens galaxies, for example produced by sub-haloes within the main dark matter halo of the deflector. If present, these sub-haloes may also produce non-quadrupolar distortions to the lens image. Furthermore, there is evidence from observations (Bender et al. 1988; Stacey et al. 2024) and simulations (Naab et al. 1999) that isophotes of elliptical galaxies show octupolar distortions (so-called ‘boxyness’ and ‘diskyness’), which, it could be argued, should also be reflected in their underlying mass distribution.

One conclusion that may be drawn from this is that ‘external’ shears may be biased high due to unaccounted-for boxyness or diskyness in the deflector mass profile. We can test whether this conclusion holds for the LOS shear by adding boxyness and diskyness to our lens model and re-fitting the same lenses as already modelled with the minimal model.

A general multipolar lensing potential is given by

$$\psi(\theta) = \theta \frac{a_m}{1 - m^2} \cos[m(\varphi - \varphi_m)], \quad (13)$$

where  $\theta$  and  $\varphi$  are the radial and angular coordinates of  $\theta$ ,  $m$  is the order of the multipole,  $a_m$  is its strength and  $\varphi_m$  is the orientation angle of its main axis (Keeton et al. 2003; Xu et al. 2015). In the case of the octupole,  $m = 4$ , and the shape is called ‘boxy’ when  $\varphi_4 = \frac{\pi}{4}$  and ‘disky’ when  $\varphi_4 = 0$ . To investigate whether boxyness or diskyness can affect LOS shear measurements, we further modelled our 50 SLACS lenses with the EPL\_BOXYDISKY profile in `lenstronomy`, which adds a pure octupolar distortion on top of the elliptical power law profile (Van de Vyvere et al. 2022). We kept the other components of the lens and light models the same.

We find that, in general, the addition of the octupole to the lens mass potential does not lead to significant reductions in the LOS shear measurement; in fact, the shear measurements are typically the same or of greater magnitude than the measurements made using the EPL and minimal LOS shear model alone. The octupole strength,  $a_4$ , tends to favour large values, leading to a lens convergence with a highly octupolar shape. We show an example of the reconstruction of lens SDSSJ1020+1122 in Figure 9, using our standard EPL and minimal LOS shear model (top row) and with the addition of the octupole component (bottom row). This figure shows the reconstruction of the image, the residual difference between the reconstruction and the data, the reconstructed source, the convergence map and finally the joint posterior distribution of the LOS shear components.

The effect of the octupole is not particularly evident in the reconstruction of the image, nor in the residuals or the value of the reduced  $\chi^2$ . However, it clearly leads to a strongly octupolar convergence and a very different source reconstruction to the case of the minimal model. The increased uncertainty on the LOS shear components can also be seen in the larger  $1\sigma$  and  $2\sigma$  regions of the posterior.

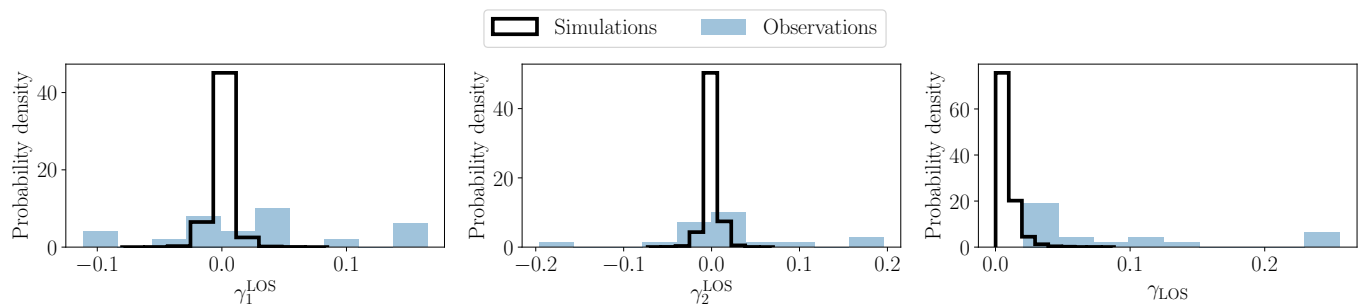


**Fig. 8.** Distribution of the LOS shear measurements from the SLACS lenses using the minimal model (solid blue) and as estimated from the RAYGALGROUPSIMS simulations (unfilled black). The left panel shows the  $\gamma_1$  component of the LOS shear, the middle panel shows the  $\gamma_2$  component and the right panel shows the LOS shear magnitude.

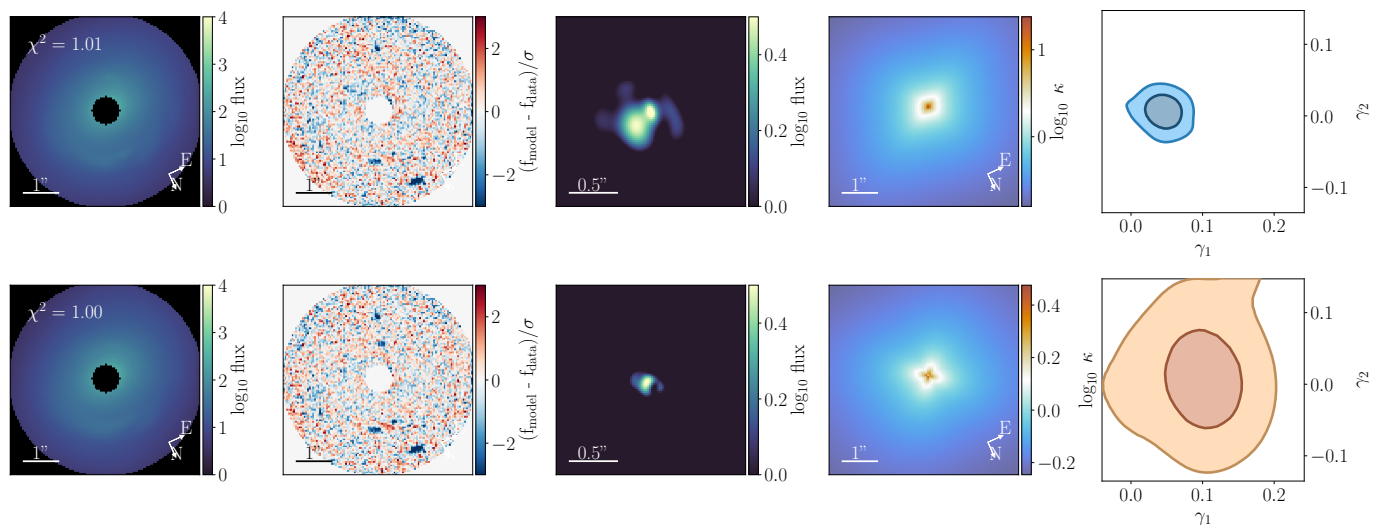


**Fig. 9.** The fit of lens SDSSJ1020+1122 with the EPL + minimal LOS shear model (top row) and the EPL + minimal LOS shear + octupole model (bottom row). From left to right, the panels show the reconstruction of the image, the residual difference between the image data and the reconstruction, the source reconstruction, the convergence map and the joint posterior distribution of the components of the LOS shear,  $\gamma_1$  and  $\gamma_2$ . The dark and light shaded areas are respectively the  $1\sigma$  and  $2\sigma$  confidence intervals.

In Figure 10, we show the distribution of the measured LOS shear in both the minimal model and the minimal model plus octupole, for the same lenses in each case. This plot provides evidence that the inclusion of an octupole in the elliptical power law does not lead to LOS shear measurements which are more in line with expectations from weak lensing, i.e. at or around the percent level, for this subset of strong lenses. From this we conclude that, if shear measurements that are in agreement with weak lensing are the goal, boxyness or diskyness should only be included in the lens model if physically well-motivated for the specific lens in question. This conclusion is supported by the comparison shown in Figure 8 of the distributions of the individual shear components from simulations and from the observed lenses, potentially pointing to a selection effect wherein the lenses studied in this and other works are those that, by chance, have larger shears than expected from weak lensing, rather than there being an underlying physical cause for the difference. We leave further consideration of this for a future work.

#### 4.4. Does lens light trace lens mass?

The dolphin pipeline allows the user to apply a prior which joins the ellipticity of the lens mass with the lens light, restrict-

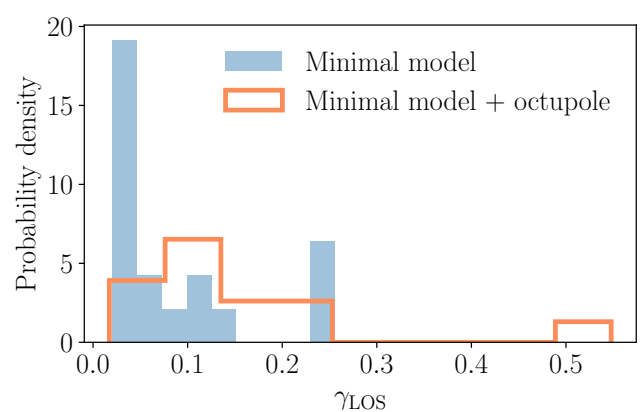


**Fig. 10.** Distribution of the LOS shear measurements in the EPL + minimal LOS shear model (solid blue) and the EPL + minimal LOS shear + octupole model (unfilled orange).

ing the differences between the axis ratios and position angles of the two components. This prior appears to be physically well-

motivated, as it is expected that the lens light traces the underlying lens mass, within some reasonable uncertainty. However, if there are strong foreground effects, the lens light will experience significant foreground lensing, meaning that it may well no longer trace the lens mass within the prior constraints. To explore this scenario, we applied the aforementioned prior in our modelling pipeline, fitting the lenses with the minimal shear model, and requiring that the lens light ellipticity of the first Sérsic profile and lens mass ellipticity position angles be within 15 degrees of each other, and that the axis ratio of the lens light and lens mass ellipticity should be the same.

In Figure 11, we show the one and two dimensional marginalised posterior distributions on the lens mass ellipticity  $e^{\text{mass}}$ , the ellipticity of the first Sérsic lens light profile  $e^{\text{light}}$ , along with the minimal model shear parameters,  $\gamma_{\text{od}}$  and  $\gamma_{\text{LOS}}$  that result from fitting the lens SDSSJ0330-0020 with our lens model, with (red contours) and without (blue contours) the ellipticity prior described above. Furthermore, we also show the posterior distributions as obtained when fitting this lens with the no foreground shear model (purple contours).

From this figure, we can see that the prior acts to confine the joint posterior of the lens mass and light ellipticity components to a small region of parameter space, as intended. However, due to the well-known degeneracy between lens ellipticity and foreground shear, this has the knock-on effect of also restricting the posteriors of the foreground shear parameters. The end result is that the LOS shear constraint for this lens changes when this prior is included, from  $\gamma_{\text{LOS}} = 0.03 \pm 0.022$  without the prior to  $\gamma_{\text{LOS}} = 0.05 \pm 0.071$  with the prior, due to the too-stringent restriction of the lens ellipticity.

Whilst these two LOS shear measurements are still consistent at  $1\sigma$ , this may not always be true, particularly in the case of large foreground shears where we expect the effect to be greater. This conclusion is borne out by the fact that the constraints on these parameters in the no foreground shear model are virtually identical to the constraints obtained in the minimal model when this prior is applied. We therefore argue that such priors should always be avoided when shear measurements are attempted. We have shown a single example here but this effect can be seen in all the lenses where the minimal model was successful.

## 5. Conclusions

In this work, we modelled a selection of 50 of the SLACS strong lenses, aiming to robustly measure the LOS shear for the first time. We used a lens model which consisted of an elliptical power law profile for the main deflector, two Sérsic profiles for the lens light, and a Sérsic plus shapelets for the source. On top of this, we modelled the LOS shear using the minimal model of Fleury et al. (2021). We found that, of these 50 lenses, only 18 were successfully fit with this model, with the majority of rejected fits being due to strong residuals between the best-fit model and the data, indicative of an overall poor lens model. We found that the distribution of our LOS shear magnitude measurements is consistent with those in the recent literature, obtained using the usual ‘external’ or ‘residual’ shear model.

We examined the effect of neglecting the post-Born corrections to the main deflector due to foreground shear and the LOS rotation in our model, re-fitting the same lenses with these parameters fixed to zero. We found that the degeneracy present between the lens mass ellipticity and the foreground shear is propagated to the LOS shear, and for certain individual lenses this leads to significantly different LOS shear measurements. How-

ever, considering the sample as a whole, this bias appears to average out for small shear magnitudes.

We also fitted our lenses with a further degree of freedom in the lens mass model, allowing for octupolar distortions, i.e. boxyness and diskyness. We found that this leads to larger LOS shear magnitudes in general, and in some specific cases, significantly different constraints on the LOS shear parameters to those found using the minimal model.

Lastly, we investigated the use of a prior which joins the lens mass and lens light ellipticities. We found that this prior has the same effect on LOS shear measurements as the removal of foreground shear from the model, with shear measurements becoming biased compared to the minimal model. This is due to the prior introducing extremely tight constraints on the lens mass ellipticity, which propagates to the LOS shear.

From this, we conclude that, if shear measurements are the goal of a lens modelling programme, the minimal line-of-sight model must be used. It is too risky to neglect the foreground shear for the sake of marginally faster posterior sampling, unless the foreground is known to be insignificant. This may be true for isolated strong lens systems but is likely not the case for lenses in dense environments. We note that this conclusion may be dependent on the choice of lens mass model, and may not hold for inference performed with a different model to the elliptical power law used in this work.

It is also clear that the question of whether the total magnitude of the LOS shear parameter is produced by line-of-sight effects remains open. We found LOS shear measurements in good agreement with external shear measurements from the recent literature, which are known to be larger than weak lensing shear estimated around strong lenses (Etherington et al. 2024), as well as those from simulations, as discussed above. This is the key point we wish to emphasise: given the agreement between our findings and those of previous works, we conclude that the lines of sight of the SLACS strong lenses studied in this work are well-characterised and modelled. It is the modelling of the main deflector to which attention must now be devoted, if the cosmological shear signal is to be disentangled from the contribution of the lens. However, our results also show that adding boxyness and diskyness to the lens mass model is not the panacea that might have been expected, at least for the strong lenses modelled in this work. Whether any further complexity can be added to mass models that is still physically well-motivated remains to be seen.

In conclusion, the task of uniformly modelling a very large catalogue of strong lenses and obtaining accurate shear measurements for the purposes of cosmology will clearly not be achieved with current data or modelling techniques. Lens model constraints may be improved using image data in which the lensed source light is more easily separable from the lens light; this may be seen in James Webb Space Telescope (JWST) imaging of high-redshift lensed sources e.g. Mercier et al. (2024) – since JWST observes in the near and mid-infrared, it has a much higher signal-to-noise ratio for redder sources compared to e.g. HST. Furthermore, more work must be done to build lens models which accurately match the physical complexity of strong lens galaxies.

*Acknowledgements.* We are very grateful to Théo Dubosq, Pierre Fleury and Giacomo Queirolo for useful discussions throughout the preparation of this work and for their insightful comments on the manuscript.

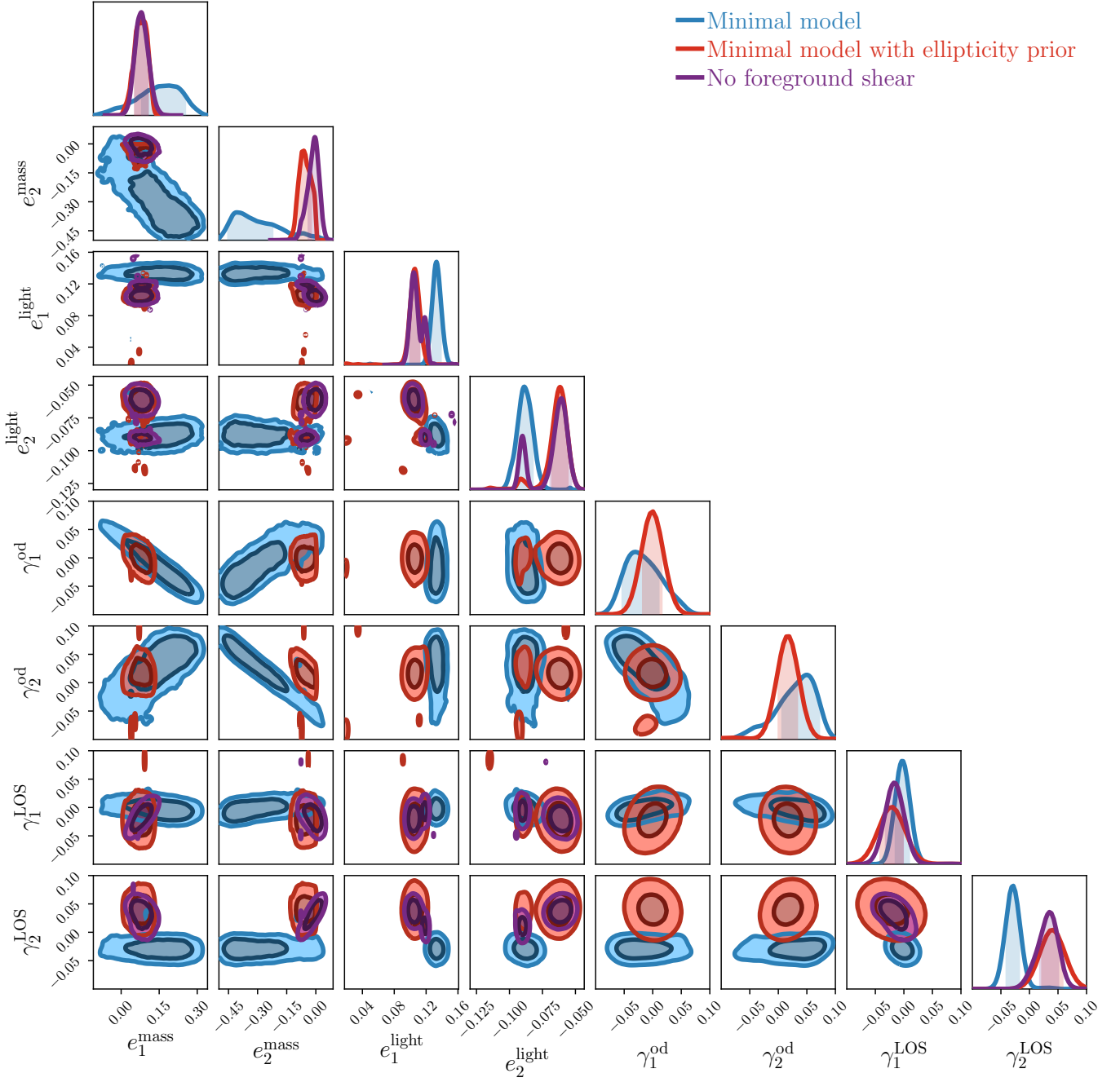


**Fig. 11.** The one and two dimensional marginalised posterior distributions on the lens mass ellipticity, lens light ellipticity, foreground shear and LOS shear parameters obtained by fitting the minimal model to lens SDSSJ0330-0020, both with (red contours) and without (blue contours) the prior that joins the lens light and mass ellipticities, and with the no foreground shear model (purple contours). Dark and light shaded regions represent the  $1\sigma$  and  $2\sigma$  confidence intervals respectively.

## References

- Anderson, T. W. & Darling, D. A. 1952, *The Annals of Mathematical Statistics*, 23, 193
- Andrae, R., Schulze-Hartung, T., & Melchior, P. 2010, arXiv e-prints, arXiv:1012.3754
- Avila, R. J., Hack, W., Cara, M., et al. 2015, in *Astronomical Society of the Pacific Conference Series*, Vol. 495, *Astronomical Data Analysis Software and Systems XXIV (ADASS XXIV)*, ed. A. R. Taylor & E. Rosolowsky, 281
- Bender, R., Doebereiner, S., & Moellenhoff, C. 1988, *Astronomy & Astrophysics Supplement*, 74, 385
- Bezanson, R., van Dokkum, P. G., Franx, M., et al. 2011, *The Astrophysical Journal: Letters*, 737, L31
- Birrer, S. & Amara, A. 2018, *Physics of the Dark Universe*, 22, 189

- Birrer, S., Amara, A., & Refregier, A. 2015, *The Astrophysical Journal*, 813, 102
- Birrer, S., Millon, M., Sluse, D., et al. 2024, *Space Science Reviews*, 220, 48
- Birrer, S., Shajib, A. J., Gilman, D., et al. 2021, *Journal of Open Source Software*, 6, 3283
- Birrer, S., Welschen, C., Amara, A., & Refregier, A. 2017, *Journal of Cosmology and Astroparticle Physics*, 04, 049
- Birrer, S. et al. 2020, *Astronomy & Astrophysics*, 643, A165
- Bolton, A. S., Burles, S., Koopmans, L. V. E., Treu, T., & Moustakas, L. A. 2006, *The Astrophysical Journal*, 638, 703
- Chae, K.-H. 2010, *Monthly Notices of the Royal Astronomical Society*, 402, 2031
- Claeskens, J.-F., Sluse, D., & Riaud, P. 2006, *Astronomy & Astrophysics*, 451, 865
- de Vaucouleurs, G. 1948, *Annales d'Astrophysique*, 11, 247

- Etherington, A. et al. 2022, *Monthly Notices of the Royal Astronomical Society*, 517, 3275
- Etherington, A. et al. 2024, *Monthly Notices of the Royal Astronomical Society*, 531, 3684
- Falco, E. E., Gorenstein, M. V., & Shapiro, I. I. 1985, *The Astrophysical Journal Letters*, 289, L1
- Fleury, P., Larena, J., & Uzan, J.-P. 2021, *Journal of Cosmology and Astroparticle Physics*, 08, 024
- Foreman-Mackey, D., Hogg, D. W., Lang, D., & Goodman, J. 2013, *Publications of the Astronomical Society of the Pacific*, 125, 306
- Fuller, W. A. 1987, *Measurement Error Models* (Wiley)
- Goodman, J. & Weare, J. 2010, *Communications in Applied Mathematics and Computational Science*, 5, 65
- He, Q. et al. 2024, *Monthly Notices of the Royal Astronomical Society*, 532, 2441
- Hezaveh, Y. D. et al. 2016, *The Astrophysical Journal*, 823, 37
- Hinton, S. R. 2016, *The Journal of Open Source Software*, 1, 00045
- Hogg, N. B., Fleury, P., Larena, J., & Martinelli, M. 2023, *Monthly Notices of the Royal Astronomical Society*, 520, 5982
- Johnson, D., Fleury, P., Larena, J., & Marchetti, L. 2024, *Journal of Cosmology and Astroparticle Physics*, 10, 055
- Keeton, C. R., Gaudi, B. S., & Petters, A. O. 2003, *The Astrophysical Journal*, 598, 138
- Krist, J. E., Hook, R. N., & Stoehr, F. 2011, in *Optical Modeling and Performance Predictions V*, ed. M. A. Kahan, Vol. 8127, *International Society for Optics and Photonics (SPIE)*, 81270J
- Mercier, W., Shuntov, M., Gavazzi, R., et al. 2024, *Astronomy & Astrophysics*, 687, A61
- Naab, T., Burkert, A., & Hernquist, L. 1999, *The Astrophysical Journal: Letters*, 523, L133
- Nightingale, J. W., He, Q., Cao, X., et al. 2024, *MNRAS*, 527, 10480
- Prat, J. & Bacon, D. 2025 [arXiv:2501.07938]
- Rasera, Y. et al. 2022, *Astronomy & Astrophysics*, 661, A90
- Razali, N. M. & Wah, Y. B. 2011, *Journal of Statistical Modelling and Analytics*, 2, 21
- Refregier, A. 2003, *Monthly Notices of the Royal Astronomical Society*, 338, 35
- Refregier, A. & Bacon, D. 2003, *Monthly Notices of the Royal Astronomical Society*, 338, 48
- Refsdal, S. 1964, *Monthly Notices of the Royal Astronomical Society*, 128, 307
- Sahu, N. et al. 2024, *The Astrophysical Journal*, 970, 86
- Schneider, P. & Sluse, D. 2014, *Astronomy & Astrophysics*, 564, A103
- Sérsic, J. L. 1963, *Boletín de la Asociación Argentina de Astronomía La Plata Argentina*, 6, 41
- Sérsic, J. L. 1968, *Atlas de Galaxias Australes*
- Shajib, A. J., Treu, T., Birrer, S., & Sonnenfeld, A. 2021, *Monthly Notices of the Royal Astronomical Society*, 503, 2380
- Shajib, A. J., Vernardos, G., Collett, T. E., et al. 2024, *Space Science Reviews*, 220, 87
- Sprent, P. 1998, *Data Driven Statistical Methods* (Chapman & Hall)
- Stacey, H. R., Powell, D. M., Vegetti, S., et al. 2024, *Astronomy & Astrophysics*, 688, A110
- Suyu, S. H., Auger, M. W., Hilbert, S., et al. 2013, *The Astrophysical Journal*, 766, 70
- Tan, C. Y., Shajib, A. J., Birrer, S., et al. 2024, *Monthly Notices of the Royal Astronomical Society*, 530, 1474
- Tessore, N. & Metcalf, R. B. 2015, *Astronomy & Astrophysics*, 580, A79
- Treu, T., Koopmans, L. V., Bolton, A. S., Burles, S., & Moustakas, L. A. 2006, *The Astrophysical Journal*, 640, 662
- Turner, E. L., Ostriker, J. P., & Gott, III, J. R. 1984, *The Astrophysical Journal*, 284, 1
- Van de Vyvere, L., Gomer, M. R., Sluse, D., et al. 2022, *Astronomy & Astrophysics*, 659, A127
- Vegetti, S. & Koopmans, L. V. E. 2009, *Monthly Notices of the Royal Astronomical Society*, 400, 1583
- Vegetti, S., Koopmans, L. V. E., Auger, M. W., Treu, T., & Bolton, A. S. 2014, *Monthly Notices of the Royal Astronomical Society*, 442, 2017
- Vegetti, S., Lagattuta, D. J., McKean, J. P., et al. 2012, *Nature*, 481, 341
- Wong, K. C. et al. 2020, *Monthly Notices of the Royal Astronomical Society*, 498 [arXiv:1907.04869]
- Xu, D., Sluse, D., Gao, L., et al. 2015, *Monthly Notices of the Royal Astronomical Society*, 447, 3189